HARMONI at ELT : system analysis and performance estimation of the high-contrast module

Alexis Carlotti, Laurent Jocou, Thibaut Moulin, Patrick Rabou, Alexis Bidot, Adrien Hours, Yves Magnard, Alain Delboulbé, Fabrice Pancher, Élodie Choquet, et al.

HARMONI at ELT: System analysis and performance estimation of the high-contrast module

Alexis Carlotti[a], Laurent Jocou[a], Thibaut Moulin[a], Patrick Rabou[a], Alexis Bidot[a], Adrien Hours[a], Yves Magnard[a], Alain Delboulbé[a], Fabrice Pancher[a], Élodie Choquet[b], Arthur Vigan[b], Matthis Houlé[d], Kjetil Dohlen[b], Jean-François Sauvage[b,c], Thierry Fusco[b,c], Niranjan Thatte[e], Benoit Neichel[b], Fraser Clarke[e], Dave Melotte[e], Matthias Tecza[e], Hermine Schnetler[f], and on behalf of the HARMONI consortium[e]

[a]Univ. Grenoble Alpes, CNRS, IPAG, 38000 Grenoble, France
[b]Aix Marseille Univ., CNRS, CNES, LAM, Marseille, France
[c]ONERA, The French Aerospace Lab, Châtillon, France
[d]Université Côte d'Azur, Observatoire de la Côte d'Azur, CNRS, Nice, France
[e]Department of Physics, University of Oxford, Oxford, UK
[f]United Kingdom Astronomy Technology Centre (UKATC), Edinburgh, UK

ABSTRACT

HARMONI is the first light visible and near-IR integral field spectrograph for the ELT. It covers a large spectral range from 450nm to 2450nm with resolving powers from 3500 to 18000 and spatial sampling from 60mas to 4mas. It can operate in two Adaptive Optics modes - SCAO (including a High Contrast capability) and LTAO - or with NOAO. The project is preparing for Final Design Reviews. The high-contrast module (HCM) has been designed to characterize planets as close as 100mas from their host star (goal: 50mas), and presenting a 1e-6 flux ratio with it. To do so, it will use (1) a passive atmospheric dispersion corrector, (2) a set of amplitude apodizers and focal plane masks to lower the diffracted intensity next to the star and attenuate the PSF core, (3) a dedicated Zernike wavefront sensor to track the non-common path aberrations with the SCAO subsystem at a 0.1Hz frequency, and (4) post-processing algorithms that will rely on the temporal and spectral diversity of the IFS data to separate the planetary signals from the noise. This communication details several trade-off analyses involved in the co-design of the hardware of the HCM. It also presents contrast performance estimates that have been derived through an analysis of post-processed, simulated IFS data obtained with an end-to-end numerical model of the HCM and the rest of HARMONI. The respective interests of ADI and molecular mapping are compared in this specific case.

Keywords: ELT, Spectroscopy, high spectral resolution, high angular resolution, direct imaging, exoplanets

1. INTRODUCTION

HARMONI[1] will be a general purpose instrument of ESO's Extremely Large Telescope (ELT) observing in the visible and the near-infrared with an integral field spectrograph. It will study a large variety of objects, from small bodies in the solar system, to galaxies in the early universe, and one of its top level requirements is to characterize exoplanets with a flux ratio with their host star down to 10^{-6}, and located as close as 0.2".

Imaging exoplanets is difficult because of this combination of short angular separation, and high flux ratio (or contrast). Indeed, the planet is hundreds to thousands of times fainter than the residual light of the star at the separation where it must be observed. This residual light is both induced by aperture diffraction effects, and by the wavefront aberrations induced by the atmosphere, and by the optics.

Because of the many science cases that HARMONI will address, it cannot be designed to observe exoplanets in the same way that instruments such as VLT-SPHERE,[2] GPI,[3] SCExAO,[4] and MAGAO-X[5] have been.

Further author information: (Send correspondence to Alexis Carlotti)
A.C.: E-mail: alexis.carlotti@univ-grenoble-alpes.fr

Enabling an integral field unit (IFU) like HARMONI to efficiently observe exoplanets is possible, however. In fact, it has recently been suggested, and then demonstrated on sky, that IFU with a high enough resolving power, say, a few thousands, could quite efficiently be used to detect exoplanets,[6–8] and that, combined with a high-Strehl adaptive optics (AO) system, and a coronagraph, they could potentially detect planets that current direct imaging instruments cannot.

Enabling HARMONI to perform these high-contrast observations while adding as little constraints as possible to the overall design of the instrument will be the task of the high-contrast module (HCM). Using the single conjugated AO (SCAO) subsystem of HARMONI that provides diffraction-limited point-spread functions (PSF), the HCM will:

- reduce the atmospheric dispersion using a passive atmospheric dispersion corrector (ADC) optimized for a single zenith distance,
- lower the amplitude of the non-common path aberrations (NCPA) between the SCAO subsystem and the HCM using a ZELDA[9] wavefront sensor (WFS) that will measure phase aberrations between 1.15 and $1.20\mu m$, leaving the light above $1.25\mu m$ for science observations,
- lower the diffracted light around the star using a set of shaped pupil apodizers,[10]
- strongly attenuate the core region of the PSF using a set of focal plane masks (FPM).

Finally, an additional calibration of the low-order NCPA between the HCM and the science detector will be performed using detector data.

HARMONI will operate in pupil tracking mode when high-contrast observations are performed with the HCM. There are two reasons for that: (1) it is necessary to keep the speckle pattern induced by the NCPA fixed on the detector so that it can be removed as efficiently as possible in post-processing, and (2) apodizers must be aligned with respect to the telescope pupil.

This paper presents the results of the system analysis that was performed when designing the HCM, and its expected performance derived from the analysis using post-processing algorithms of simulated datacubes obtained from a numerical model of HARMONI and of the HCM.

Section 2 recalls the functional analysis of the HCM, and provides an updated short overview of its design. Section 3 details the system analysis that was carried out to converge towards the specifications of the HCM. Section 4 presents the expected performance of the HCM. A conclusion is provided in sec.5.

2. FUNCTIONAL ANALYSIS AND DESIGN OF THE HCM

A first version of the design of the HCM was previously presented,[11] and an updated, in-depth description of the design is presented in the same conference as the present paper. Apart from the ADC mentioned in sec.1, and which was not part of the previous design, the functions that have been listed have not changed, although important modifications have been made to the opto-mechanical design of the HCM.

The HCM will be located in the natural guide star system (NGSS) of HARMONI, which is itself located between the optical relay, and the cryostat that contains the IFS and its pre-optics. When high-contrast observations will be performed, the HARMONI pick off unit (HPO) will be deployed immediately after the SCAO dichroic, which will transmit light above $1\mu m$. A fold mirror in the HPO will send the beam towards the high-contrast bench (HCB). Light is processed in the HCB and returned towards the HPO, which focuses it and folds it towards the IFS. This is illustrated in fig.1.

A few core functions must be performed by a high-contrast imaging subsystem such as the HCM.

One function is to lower the diffracted intensity of the light around the star so as to reduce both the photon noise and the amplitude of the pinned speckles that can prevent the detection of a planet. This is usually done using a coronagraph, i.e., a series of pupil and focal plane masks whose combination actively attenuates the diffracted light while letting through as much light of the planet as possible.

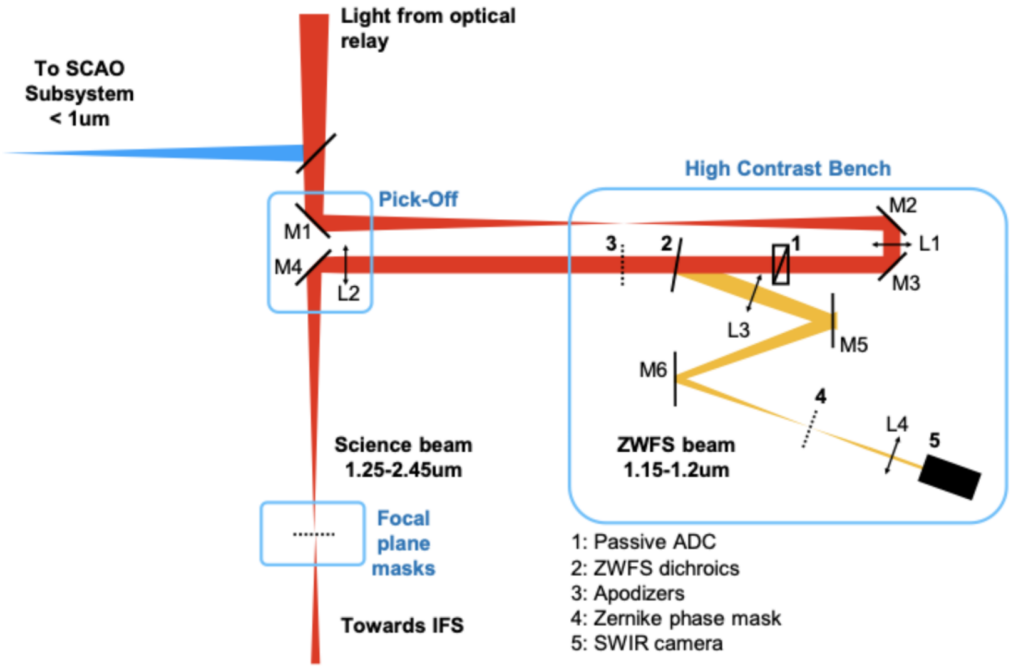

Figure 1: Schematic view of the HCM. A converging beam coming from the top is intercepted in the NGSS right after the SCAO dichroic by the HPO, and sent towards the HCB, before being returned towards the HPO, and sent to the IFS which is located at the bottom. On its way towards it, FPM are used to block the core of the PSF. Light in the 1.15-1.2μm spectral range is used by the ZELDA WFS (ZWFS).

Because the atmospheric dispersion is not corrected at the instrument level in HARMONI, it is not possible to rely on a focal plane mask to actively attenuate the diffracted light. A full ADC could have been added to the HCM to change this, but a less invasive solution was chosen instead: shaped pupil amplitude apodizers. This type of pupil plane mask is not affected by residual dispersion, although it still requires an FPM to block the core region of the PSF. Shaped pupils will be used by the SHARK-NIR instrument at LBT,[12] and some will be part of the coronagraphic instrument of the Nancy Grace Roman Space Telescope (NGRST[13]).

A second core function is to limit as much as possible the NCPA between the WFS of the adaptive optics system and the science detector. The origin and properties of NCPA are presented in more details in sec.3, and it is sufficient to say here that to minimize the NCPA, it is necessary to add a dedicated WFS that analyses the wavefront as close as possible to the FPM, and in a spectral range as close as possible to the spectral range of the science observations.

A ZELDA[9] WFS was chosen because of its nanometric precision, its capability to sense differential piston errors (such as island and low-wind effects), and its high spatial resolution. Indeed, since this WFS images the pupil plane, it can be used as a reference for the alignment of the apodizers. A ZELDA WFS uses a small, $1\lambda/D$ large focal phase mask to induce a $\pi/2$ phase shift in the central region of the PSF. Once the star is aligned on the center of this mask, the wavefront errors (WFE) present in the entrance pupil plane are converted into intensity aberrations that can be measured in a reimaged pupil plane.

The third core function is to mask the core region of the PSF using a FPM so that is does not saturate the detector. An alternative, and unsatisfying solution would be to use sufficiently short exposures, but the read noise of the detector would have a strong impact on the detection capability of the instrument. Since the FPM is not here used to actively attenuate the diffracted light, it can simply attenuate the PSF core instead of blocking it entirely. This has the advantage of enabling the astrometry and the spectro-photometry of the star without having to move out the FPM.

The PSF is elongated because of the atmospheric dispersion, and so must be the FPM. The ELT being almost

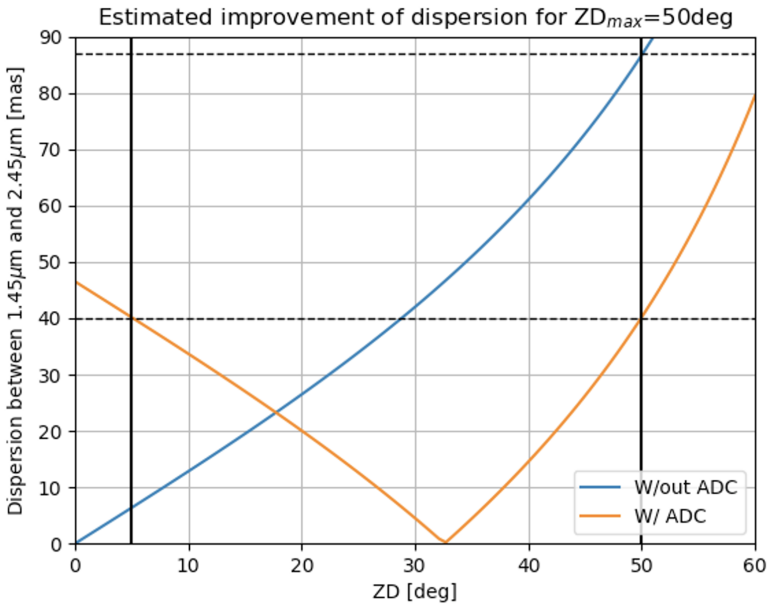

Figure 2: Atmospheric dispersion (blue line), and atmospheric dispersion residuals (orange line) in the 1.45-2.45μm spectral range as a function of the zenith distance. The dashed line indicates the residual dispersion at ZD=50deg, which is the maximum ZD for the HCM. Dispersion is lowered for ZD ¿ 17deg, and increased otherwise. Since the same FPM are used for all ZD, a net gain in minimum separation is obtained thanks to the ADC even for ZD lower than 17deg.

five times larger than the 8m telescopes of the VLT, dispersion is five times more critical. This limits the effective minimum separation at which planets can be detected. This is also an issue for the ZELDA WFS, which should ideally analyze the light of a star that is not dispersed at all. Dispersion induces a systematic bias akin to a 1D defocus that must be taken into account, and - assuming it is - still limits the efficiency of the WFS by increasing the photon noise.

These two reasons motivated the addition of an ADC, which is the fourth main function performed by the HCM. This ADC does not have to fully correct for the atmospheric dispersion, however. A *passive* ADC optimized for a single zenith distance (ZD) and which does not require any moving mechanism since the HCM requires pupil tracking mode is enough to achieve a residual dispersion that is more than twice as low as the original dispersion in the ZD range chosen for the HCM, as illustrated in fig.2.

The ZD range of the HCM was chosen to be 5-50deg. Observing planets at a higher ZD, say ZD=60deg, is quite difficult because of strong atmospheric turbulence, and large airmass. The ZD=50deg maximum was chosen so that even the HR8799 system could be observed up to a few hours from meridian. No major planetary system visible from the southern hemisphere requires a larger ZD. This is illustrated in fig.3.

The HPO also returns the beam towards the IFS, and focuses it with the right magnification so that images can be Nyquist sampled at 1.45μm, or for a slightly smaller wavelength.

3. SYSTEM ANALYSIS

This section goes through the main logic behind the system analysis of the HCM, and details the specific trade-offs that have been studied to converge towards the specifications of the components of the HCM.

3.1 Detection limit assumptions

The detection limit that can be achieved with a high contrast instrument depends, among other things, on the algorithms that are used to process the pre-processed data so as to extract the signal of the planet from the noise that can prevent its detection.

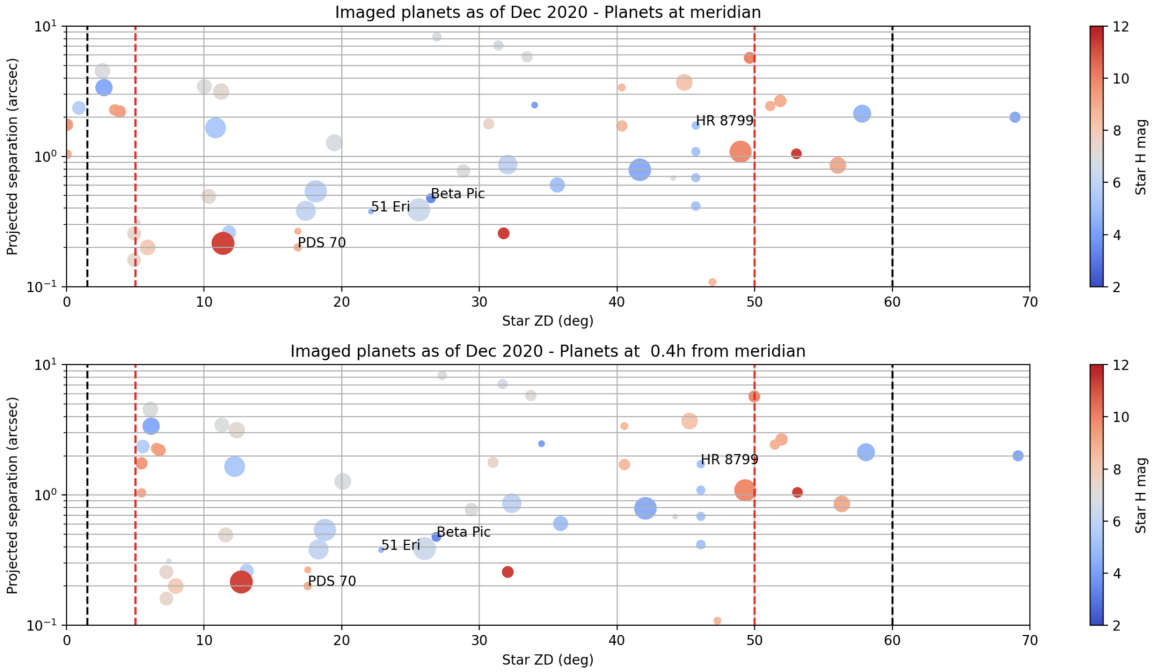

Figure 3: ZD-separation plots of stars around which planets have been imaged, at meridian (top) and 0.4h from meridian (bottom).

To do that, post-processing algorithms use diversity in the data. For instance, angular differential imaging (ADI) uses the temporal diversity of the data, while spectral differential imaging (SDI) and molecular mapping use the spectral diversity of the data.

Current instruments such as VLT-SPHERE mostly rely on ADI, and the system analysis of HARMONI assumes that it will be the case with this instrument too, even though other algorithms such as the more recently developed molecular mapping algorithm will also be applicable to the data.

When using ADI, and assuming that a good enough Strehl ratio is provided by the SCAO subsystem, the detection is ultimately limited by the relative intensity of the NCPA-induced quasi-static speckles. They vary both too slowly to be averaged, and too fast to be considered as static.

ADI uses the apparent rotation of the planet around the star with the parallactic angle to differentiate the planet from the speckle field. The efficiency of this technique varies quite a lot, and we assume hereafter that, on average, planets with a 10^{-6} flux ratio, to be detected, require the quasi-static speckles to limit the contrast in a single image without atmospheric AO residuals to 10^{-5}. We refer to this contrast as the *raw contrast*.

This specification is the basis for the optical error budget that we derive in the next sections.

3.2 Nature and properties of the NCPA

It is essential to understand the origin and the nature of the NCPA to properly constrain their impact on the raw contrast. By definition NCPA are differential wavefront aberrations that result from a difference in the wavefront that is sensed by the WFS, and the wavefront that induces speckles in the detector image.

Both the WFS and the science channel use two different sets of optics to form an image, thus inducing basic NCPA. In addition, wavefront aberrations may be chromatic. Since the WFS usually operates at a wavelength that is different from the science wavelength, this chromaticity also induces chromatic NCPA. Lag error may also have to be considered, even though the lifetime of quasi-static aberrations is much larger than those of atmospheric speckles.

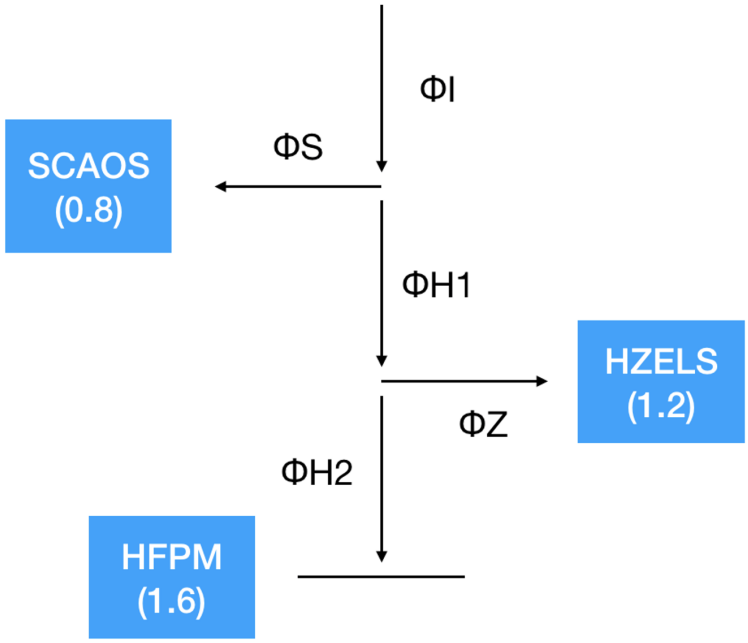

Figure 4: WFE at the origin of NCPA in the HCM. Five groups of WFE are represented: Φ_I is induced by optics located upstream of the SCAO dichroic. Φ_S is induced by the SCAO subsystem optics. Φ_{H1} is induced by optics located upstream of the ZELDA WFS dichroic. Φ_Z is induced by the optics of the ZELDA WFS. Φ_{H2} is induced by optics located downstream of the ZELDA WFS dichroic, up to the focal plane where the FPM are located.

The HCM in HARMONI faces these three types of NCPA. As illustrated in fig.4, NCPA are induced by several groups of WFE. Once sensed by the ZELDA WFS at $1.2\mu m$, and corrected by SCAO, the NCPA between the ZELDA WFS and the plane of the FPM reduce to:

$$NCPA = \Delta\Phi_I(1.2, 1.6) + \Delta\Phi_{H1}(1.2, 1.6) + \Phi_{H2}(1.6) - \Phi_Z(1.2), \tag{1}$$

where $\Delta\Phi_X(\lambda_1, \lambda_2)$ denotes the chromatic NCPA related to the difference of the Φ_X WFE between the wavelengths λ_1 and λ_2.

The Φ_S WFE disappear since they are sensed by the ZELDA WFS, but the Φ_I WFE do not, as they induce chromatic NCPA. This group includes the optics of the optical relay of HARMONI, but also the optics of the telescope. While the former can - to some extent - be constrained to satisfy our contrast requirement, the latter cannot.

A calibration of the low-order (LO) NCPA, say the first 36th Zernike modes, will be performed using the images of the science detector. That specific number of modes is related to the deformable mirror (DM) of the calibration unit of HARMONI, which will be a 97-15 ALPAO DM with 11 actuators across. Once that calibration is performed, the ZELDA WFS will have to work with a WFE offset similar to the LO part of the NCPA detailed in eq. 1.

For chromatic NCPA to be zero, chromatic dispersion has to be zero too. This is not the case in HARMONI, and the footprint of the beam shifts over the optics with the wavelength, thus inducing chromatic aberrations. There is one single exception: optics located in the pupil plane do not induce chromatic NCPA.

The impact of chromatic NCPA, and basic NCPA on the contrast is different. This is illustrated in fig.5. In the latter case, it also depends a lot on the conjugated height of the optics, i.e., its distance to the pupil plane.

This points out the necessity to consider the specific optical layout of HARMONI, and of the HCM, when specifying the optical surface quality of each the optics.

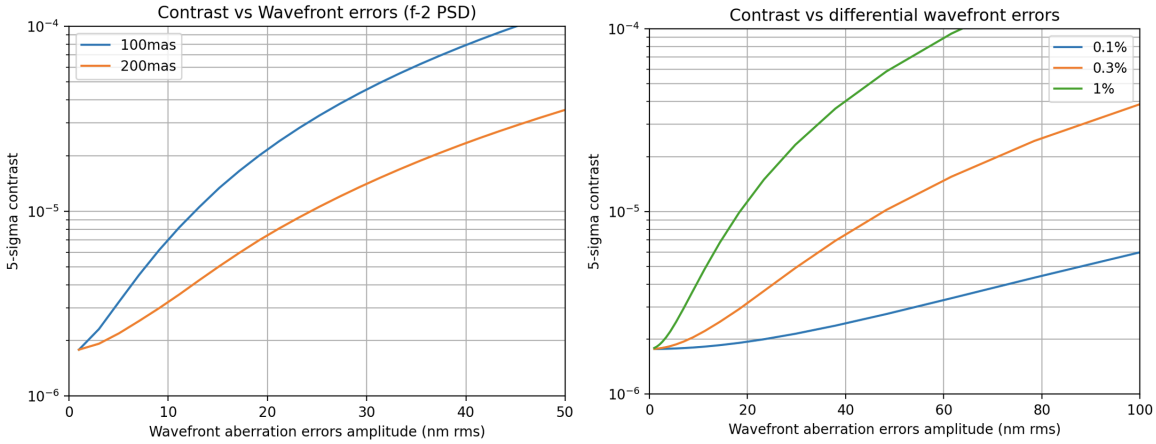

Figure 5: Contrast limit as a function of the WFE due to basic NCPA (left), and chromatic NCPA (right). In the left plot, two angular separations are considered, and a 10^{-5} contrast is for instance obtained at 200mas for a 22nm RMS WFE. In the right plot, three shift ratios are considered, illustrating the difference between optics located close or far from the pupil plane.

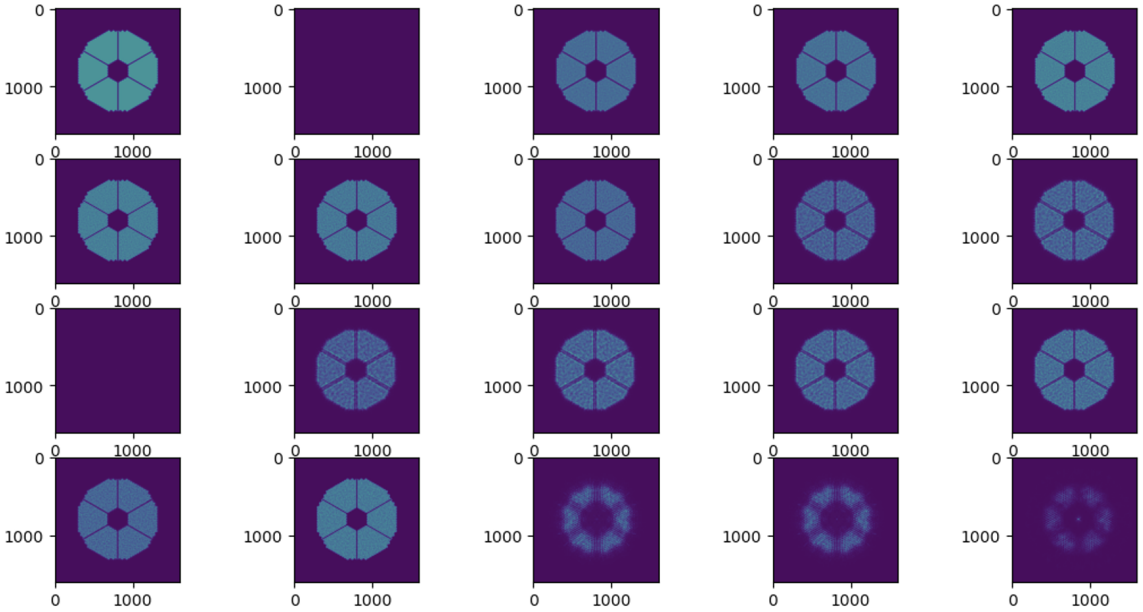

Figure 6: Beam intensity on the surface of each optics, as seen from the FPM, modeled through PROPER.[14] The two seemingly dark plots correspond to focal planes where there is in fact no optics. The last three plots correspond to optics located after the apodizer. The diffraction effects that can be seen in the plots are stronger for optics further away from the pupil, with the last plot showing the most. It corresponds to the cryostat window, an optics located quite close to the focal plane where the FPM are located.

3.3 Surface error budget

Two models have been used to specify the optical surface quality of the optics: (1) a ray optics model that associates the conjugated height of the optics that induce chromatic NCPA and the WFE that they must introduce to satisfy a given contrast constraint, and (2) a diffractive model based on the PROPER[14] Python package that directly computes the contrast for a given set of WFE. An example of the PROPER model is given in fig.6.

The impact on contrast of optical surface errors depends greatly on the PSD of these errors. We assumed in

this study that the PSD of all optics followed an f^{-2} power law, where f is the spatial frequency. This may be a conservative assumption, as high quality polishing techniques may provide PSD with $f^{-2.5}$ or f^{-3} PSD. If this type of optics are eventually used, the result will be a lesser impact on the contrast of their surface errors.

Another assumption that we have made is related to the optical surface quality of the telescope optics. They only induce chromatic NCPA, and, fortunately, the conjugated height of most of these optics is so low that their impact is negligible. Only M6 is located far enough from the pupil to matter. Private exchanges with ESO have indicated that a 40nm RMS transmitted WFE can be expected for this optics, and we have used this number in our computations.

Both models provided consistent results, although the surface quality derived from the diffractive model were 10-15% higher. In both cases, the same assumption was made that each optics should have the same impact on the contrast. These models may be modified in the future to allow some optics to have a larger impact, at the price of stronger constraints on other optics.

These results only provide the transmitted WFE associated with the beam footprint for each optics. They must be translated into surface quality errors as a function of the type of optics (refractive or reflective). The question of translating them in terms of surface errors for the entire optical surface is also relevant, especially for the optics located upstream of the HCM, which are designed for the large field of view of HARMONI, and which can be several times larger than the footprint.

Manufacturers do not require to have this information, however, and we intend to provide them with the requirements associated with a given beam footprint located at the center of the optics. These requirements will be described as both a global error, and a series of errors for low-order (LO, first 36th Zernike modes), mid-order (MO, up to 40cyc/pup), and high-order (HO, up to 80cyc/pup) aberrations. They correspond, respectively, to aberrations that will be calibrated using the DM of the calibration unit, aberrations that will have an impact within the AO correction radius of the M4, and aberrations that may have an impact in the rest of the field of view of HARMONI during high-contrast observations.

In practice the transmitted WFE that have been derived from our models are on the order of 13-25nm RMS for the optics of the optical relay, except for the cryostat window that is not seen by any wavefront sensor, and for which a 7nm RMS is required over the beam footprint. Since it is close to the image plane, however, this requirement may not be difficult to satisfy. The transmitted WFE that is acceptable for each of the optics of the HCM is 5-11nm RMS.

A median raw contrast of the apodized PSF was computed based on these transmitted WFE. A hundred realizations of randomly generated sets of wavefront error maps have been used to measure the deviation that can be expected. As illustrated in fig.7, a $1.7\,10^{-5}$ contrast is achieved at $20\lambda/D$, and it is slightly above a $2\,10^{-5}$ at $7\lambda/D$.

It may be interesting to note that the surface aberrations of each optics do not impact the contrast in the same way. This is related to two main factors: whether these optics induce chromatic NCPA or basic NCPA, and whether they are close or far away from the pupil plane.

The PROPER model was also used to study how the NCPA evolve over time. Their evolution is due to two factors: (1) all optics of the optical relay except for the cryostat window do not track the pupil, and thus rotate with the parallactic angle, and (2) the star ZD changes over time, inducing a change in the chromatic beam shift. Fig.8 illustrates this evolution for the 3 spatial frequency ranges, and MO aberrations are expected to change by 5nm RMS after 3min. The evolution shown here was computed in the specific of a star close to the maximum ZD for which the HCM will operate. The same computation was performed for stars with different ZD, or observed a few hours from meridian, and the same overall trend was observed. This can be used to set a reference exposure time for the sensing of the NCPA.

3.4 ZELDA WFS for NCPA sensing and pupil alignment

Three aspects of the ZELDA WFS have been studied as part of the system analysis: its capability to be used for pupil alignment, its precision for sensing NCPA in the specific case of HARMONI, and its capability to be used in spite of residual atmospheric dispersion.

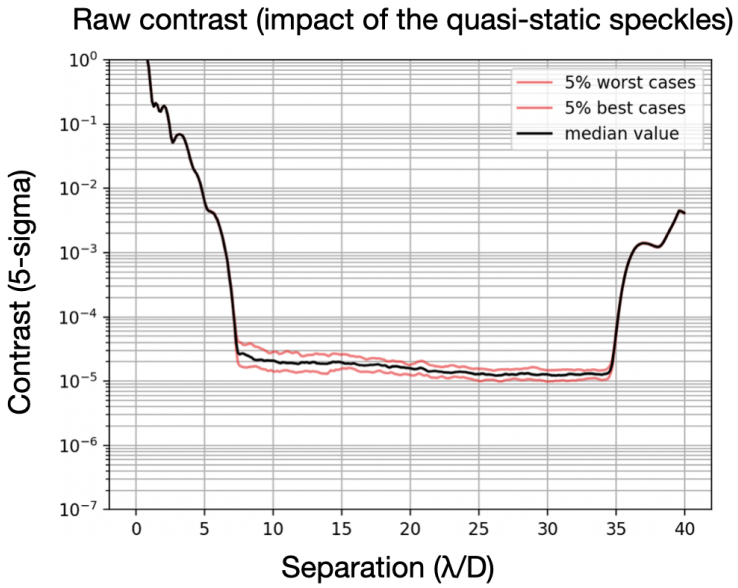

Figure 7: Raw contrast of the apodized PSF as a function of the angular separation, and based on the optical error budget.

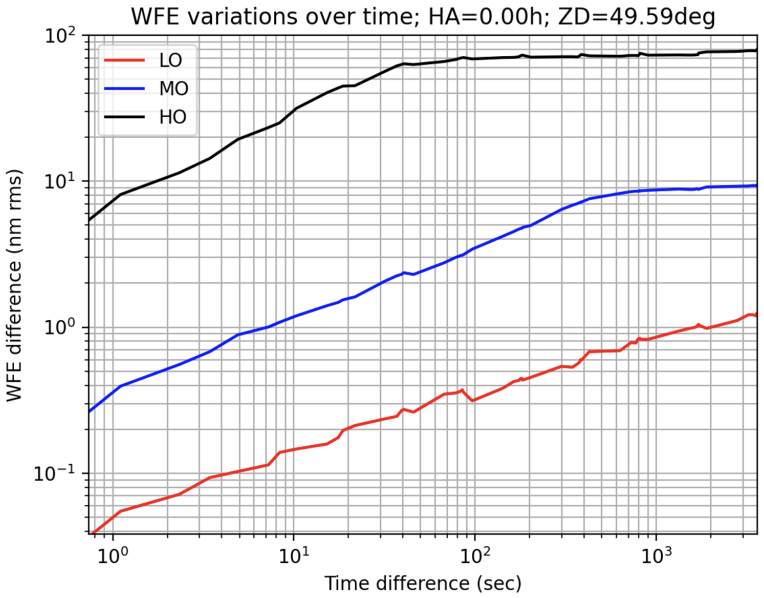

Figure 8: Evolution over time of the NCPA, i.e., differential WFE with respect to an initial WFE. MO aberrations are about ten times higher than LO, and they change by 1nm RMS after 10s, by 5nm RMS after 3min, and reach a plateau of 10nm RMS after 10min. This was computed for the ZD maximum.

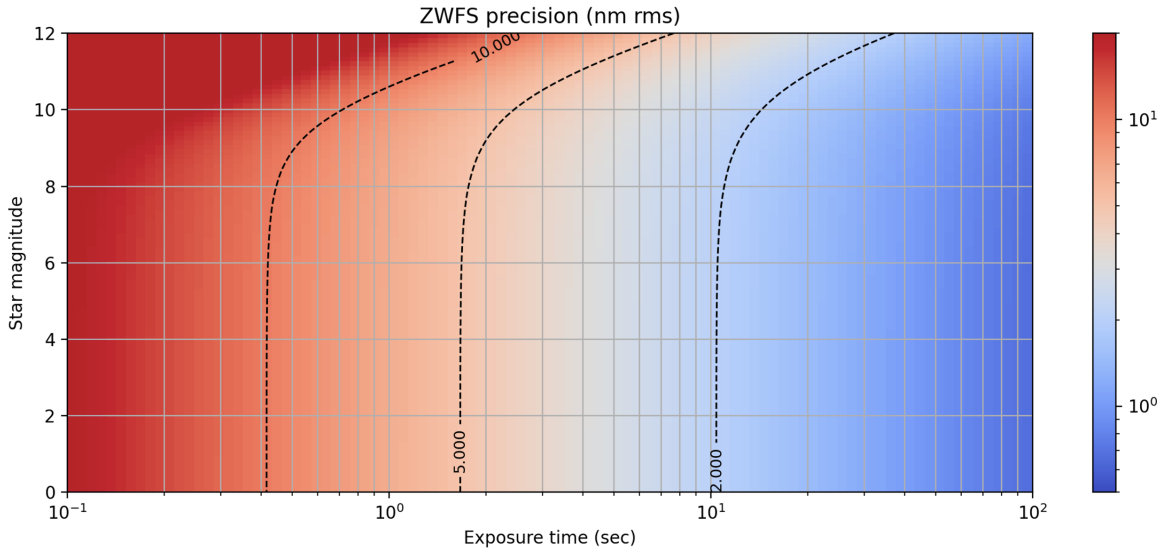

Figure 9: Expected sensing precision of the ZELDA WFS as function of the star magnitude (y-axis), and the total time over which the atmospheric AO residuals can be averaged (x-axis). The lower part of the plot corresponds to a noise regime dominated by AO residuals, while the upper part of the plot corresponds to photon-noise dominated regime.

3.4.1 Error budget of the ZELDA WFS

The physics of the ZELDA WFS is quite well known. It has been used on sky extensively with VLT-SPHERE,[9,15] as well as in the laboratory. We derived an error budget to assess the sensing precision that could be expected in the case of HARMONI, as a function of the magnitude of the star, and of the time over which the AO residuals can be averaged out. Eq.2 details the various terms of this error budget:

$$\sigma = \sqrt{\sigma_D^2 + \sigma_P^2 + \sigma_{AO}^2}, \text{ with:} \tag{2}$$

$$\sigma_D = \frac{\delta S_D}{S_0}, \tag{3}$$

$$\sigma_P = \sqrt{\frac{1}{2\,S_0}}, \tag{4}$$

$$\sigma_{AO} = \sqrt{\frac{\tau_{lag}}{T} w_{lag}^2 + \frac{\tau_{WFS}}{T} w_{WFS}^2}, \tag{5}$$

where δS_D is the readout noise of the detector (in photo-electrons per pixel), S_0 is the average intensity in the pupil (also in photo-electrons per pixel), and T is the total time over which the AO residuals are averaged out.

We assumed a conservative case for the SCAO performance: given a 20m/s windspeed, the lag error is $w_{lag} = 30nm$, and the lifetime of the phase error is $\tau_{lag} = 24ms$. The wavefront sensor error is $w_{WFS} = 110nm$, and the lifetime of the error, i.e., the lag is $\tau_{WFS} = 2ms$.

In addition, we assumed a total transmission of 0.4. This value includes a sky transmission of 0.9 (computed using ESO's skycalc in a 1150-1200nm spectral range and for a star with a ZD=50deg), a 0.8 overall reflectivity for the telescope, a 0.83 transmission for the optics of the optical relay, a 0.8 transmission for those of the HCM, and a 0.85 quantum efficiency for the SWIR detector.

Finally, we used the readout noise of the SWIR detector, which will be a C-RED2 camera from First Light Imaging, of 20e- in the high gain setting. This corresponds to an individual read, and this is likely a conservative value since exposures will be acquired in a ramp read mode for which the readout noise is less.

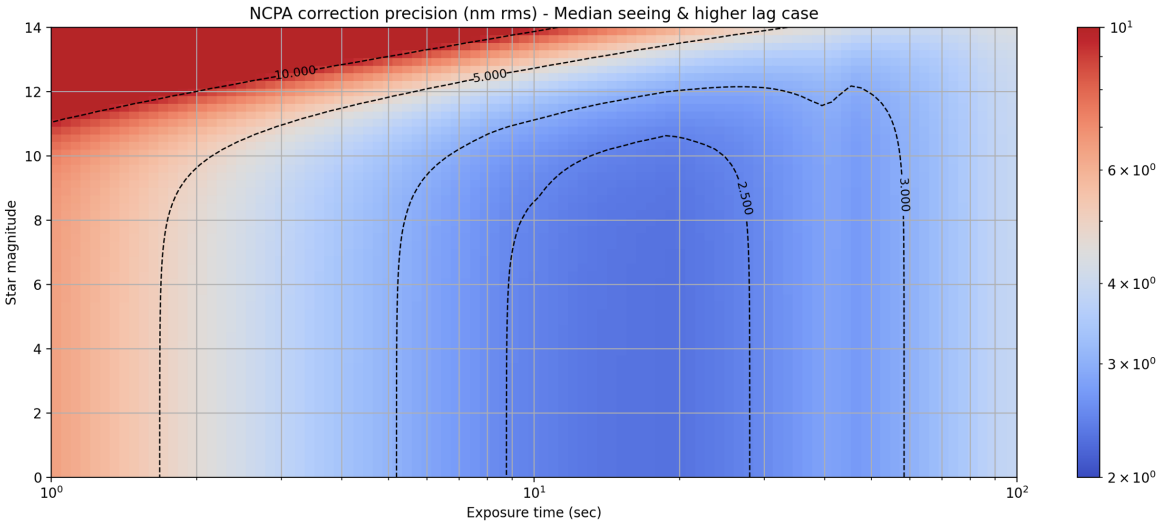

Figure 10: Expected sensing precision of the ZELDA WFS as function of the star magnitude (y-axis), and the total time over which the entire AO residuals (including quasi-static aberrations) can be averaged (x-axis). With too long averaging time, the decorrelation of the NCPA limits the sensing precision of the ZELDA WFS, and an optimal averaging time is found around 10-20s.

The pupil will be imaged over 200pixels across its diameter, so that the pupil center was be measured with a precision better than 0.2% (goal: $< 0.1\%$). Experience from previous instruments, and numerical simulations indicate that this is not a point of concern.

The result is illustrated in fig.9. A 5nm RMS precision is expected for J=0-8 stars and an averaging time of about 2s. Higher magnitude star should be observed over a longer time to achieve the same precision.

This first model, however, does not take into account the decorrelation of the NCPA over time, however. It was then modified using the results illustrated in fig.8, and the result is presented in fig.10. The main difference with the previous model is that the decorrelation of the NCPA limits the sensing precision of the ZELDA WFS in such a way that one should not average the aberrations over more than 10-20s, for which a precision of 2-3nm RMS can be achieved for J=0-10 stars. For higher star magnitudes, the precision degrades, and it is limited to 5nm RMS for J=11 stars.

The analysis was also performed for a more optimistic case of AO residuals (10m/s windspeed, $w_{lag} = 20nm$, $\tau_{lag} = 12ms$, $w_{WFS} = 90nm$, $\tau_{WFS} = 1.5ms$.). The results, which are not illustrated here, are that the optimal averaging time would be closer to 10s in that case. These numbers may evolve depending on the results of the prototyping activities around the ZELDA WFS, and later on, during the commissioning of the instrument.

3.4.2 Calibration of the dispersion bias

The residual dispersion left over after the passive ADC induces a systematic signal, i.e., a bias that must be calibrated for. Its shape, which is illustrated in fig.11a, looks like a 1D defocus term. This is not surprising since the dispersion can be seen as a continuous sum of positive and negative tilt errors.

This bias cannot be ignored when processing the images acquired with the camera of the ZELDA WFS. Fortunately, as illustrated in fig.11b, its calibration is efficient.

Without it, the difference between the original and reconstructed WFE map is different enough to prevent closing the loop when trying to correct for the NCPA. A successful laboratory demonstration of this calibration has been presented in detail in a paper of the same conference as the present paper.

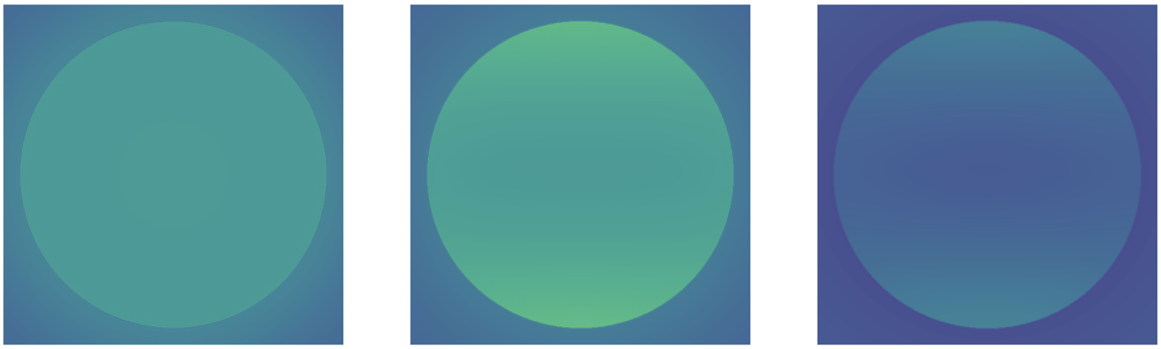

(a) Pupil intensity measured by the detector of the ZELDA WFS in the absence of WFE. Left: without dispersion. Middle: with dispersion. Right: difference.

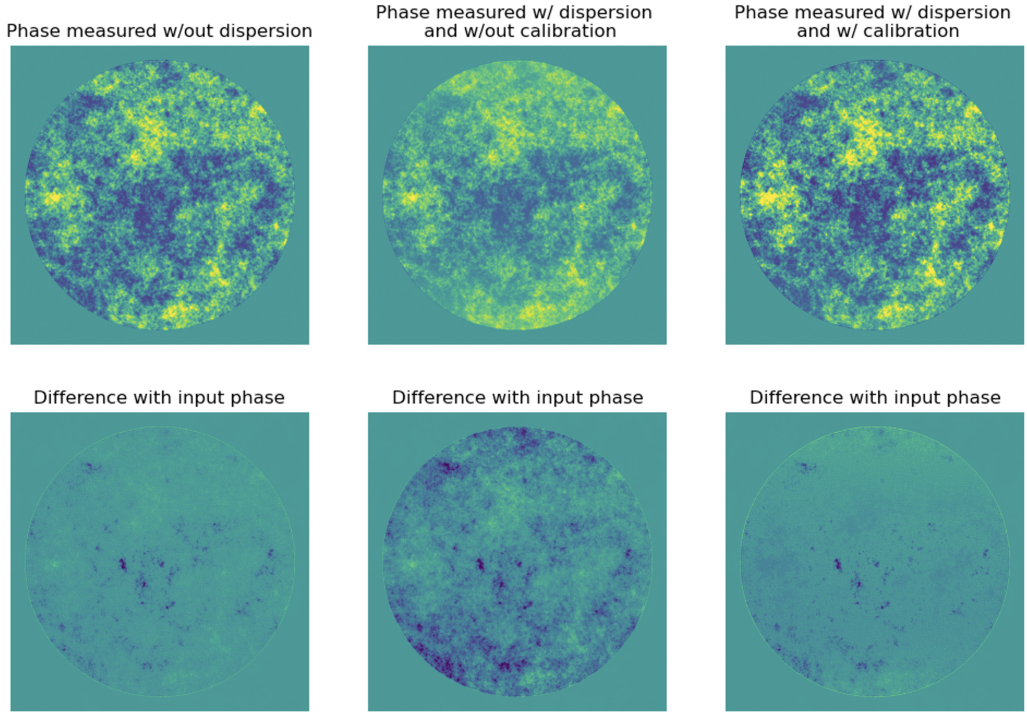

(b) Simulated wavefront sensing with the ZELDA WFS. The top and bottom rows correspond to a measured phase, and the difference with the input phase, respectively. Left plots: ideal case for which there is no dispersion. Middle plots: non-zero, non-calibrated dispersion. Right plots: non-zero, calibrated dispersion.

3.5 Design of the apodizers and focal plane masks

3.5.1 Design of the apodizers

The apodizers' objective is to attenuate the diffracted intensity next to the star, while having the highest transmission possible. They must also be robust to both lateral misalignment ($\pm 0.25\%$) and clocking misalignments (0.5deg).

Given the volume allocated to the HCM, and the number of free slots in the FPM wheel of the IFS pre-optics (3), it was decided that the HCM would carry two apodizers. The objective of the system analysis regarding these pupil masks was to come up with shaped pupils patterns that would provide complementary discovery regions around the star while satisfying the top-level requirement.

Two main assumptions were made when designing the apodizers: (1) that the residual diffracted relative intensity should be 10^{-6}, i.e., identical to the flux ratio of the faintest exoplanets that will be imaged, and (2) that they lower the diffracted intensity up to a $38\lambda/D$ separation, which corresponds to the AO control radius.

An exploration of the parameter space (minimum and maximum separations, contrast, and throughput) concluded that a 35% throughput could be achieved while satisfying the robustness, contrast, and maximum separation requirements if the minimum separation was set to $7.3\lambda/D$. By comparison, satisfying them for a $6\lambda/D$ minimum separation would result in a twice as low throughput. A $7.3\lambda/D$ minimum separation corresponds to a 96mas angular distance on sky, which satisfies the top-level requirement of HARMONI.

The HCM is designed to observe in the H and K bands. Since the PSF scales with the wavelength, it is necessary to use two FPM for each apodizer, unless the minimum separation of one in the H band corresponds to the minimum separation of the other in the K band, in which case only three FPM are required in total, and this solution was chosen given the limited number of available FPM.

The two minimum separations must have a 1.81/2.45=0.74 ratio to satisfy this constraint. This results in a $5.4\lambda/D$ minimum separation for the second apodizer. The robustness, and contrast requirements can be achieved given this minimum separation for the same throughput if the maximum separation is set to $11.5\lambda/D$.

The two apodizers (referred to as SP1 and SP2) along with their PSF are illustrated in fig.12. Their transmission is slightly above 50%. This is quite higher than their throughput, indicating that a lot of light is contained outside of the high-contrast region. A constraint was in fact set on the relative intensity of that light in a region than encompasses the whole FoV, so that this its mean value would not be higher than the maximum intensity of the AO halo in the high-contrast region, which may be as low as 10^{-4} in good seeing conditions (first quartile, 0.43").

The apodizer design may still evolve to satisfy new scientific requirements. Observing closer to the star appears to be possible, in spite of the residual dispersion, and at least one specific target offers a good reason to do so: Proxima b, which has a maximum elongation of 37mas, i.e., $3.8\lambda/D$ in H band, and would likely require a slightly smaller minimum separation of $3-3.5\lambda/D$. Favouring a minimum separation constraint over the current assumption that is made on the maximum separation, would completely change the analysis described above, however.

3.5.2 Design of the FPM

The three FPM have been chosen to globally match the core of the PSF of the SP1 and SP2 apodizers as best as possible for observations performed in all of the spectral ranges of interest for the HCM: H+K, J, H, K, H high, K1 high, and K2 high. As illustrated in fig.13, the combination of spectral ranges and apodizers leads to a large series of mask sizes. The widths and heights that are listed in this figure take into account the maximum wavelength of each of these spectral ranges, as well as the minimum separation of the apodizers, and the residual dispersion for a star observed at ZD=50deg.

FPM that should ideally be used for J band observations display a large height-to-width ratio of up to 1.5, meaning that their height can be 50% larger than their width. Note that this takes into account the effect of the passive ADC. Without it, that ratio would be far larger.

The 3 selected FPM are shown in fig.14. While FPM2 and FPM3 are almost circular, FPM1 shows a noticeable elongation. Observations in the K1 high band are the most affected by that choice since a non-negligible area

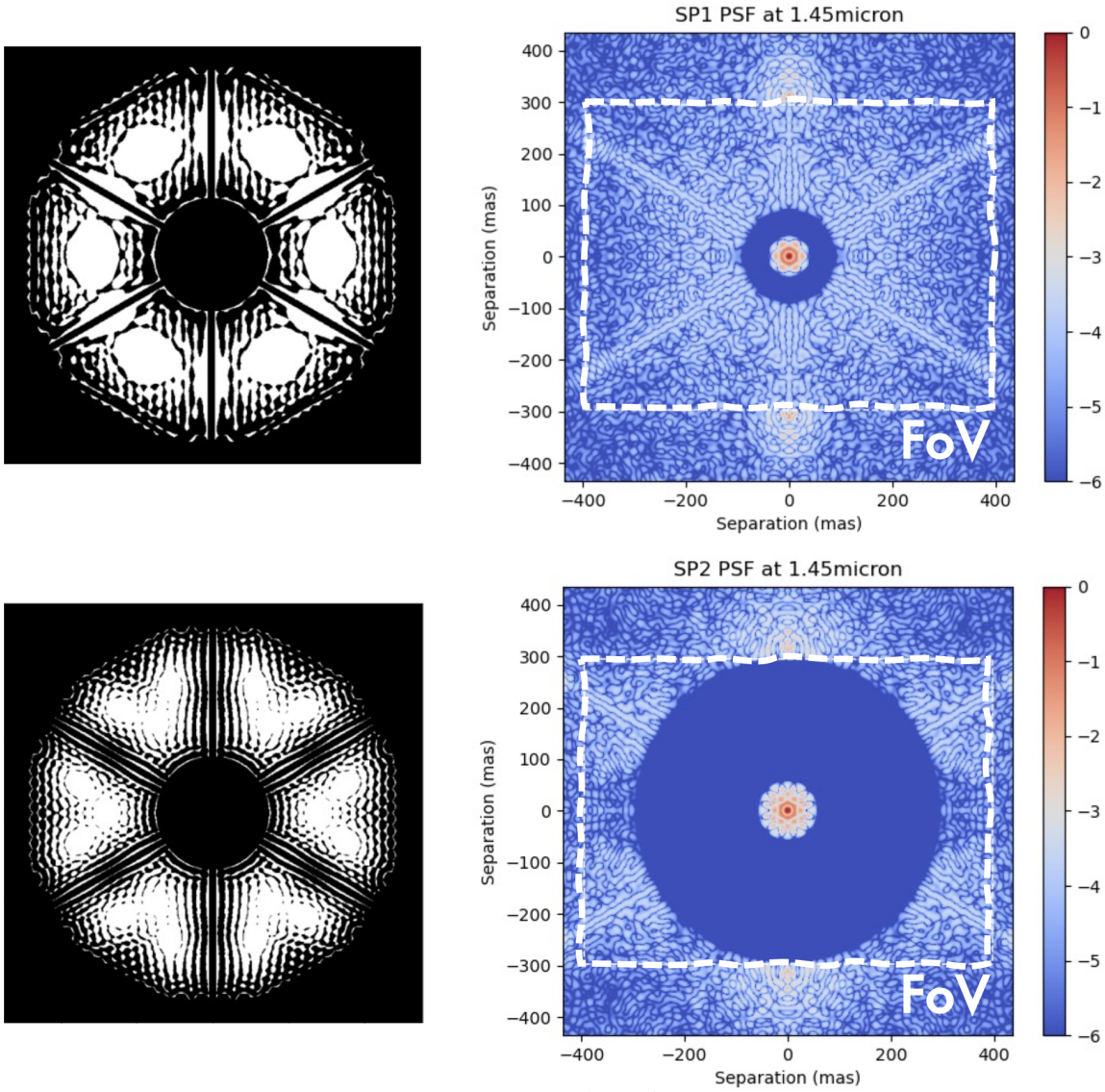

Figure 12: Transmission (left) and log-scale PSF (right) of the two shaped pupil apodizers, SP1 (top), and SP2 (bottom). The white areas let light through the apodizers.

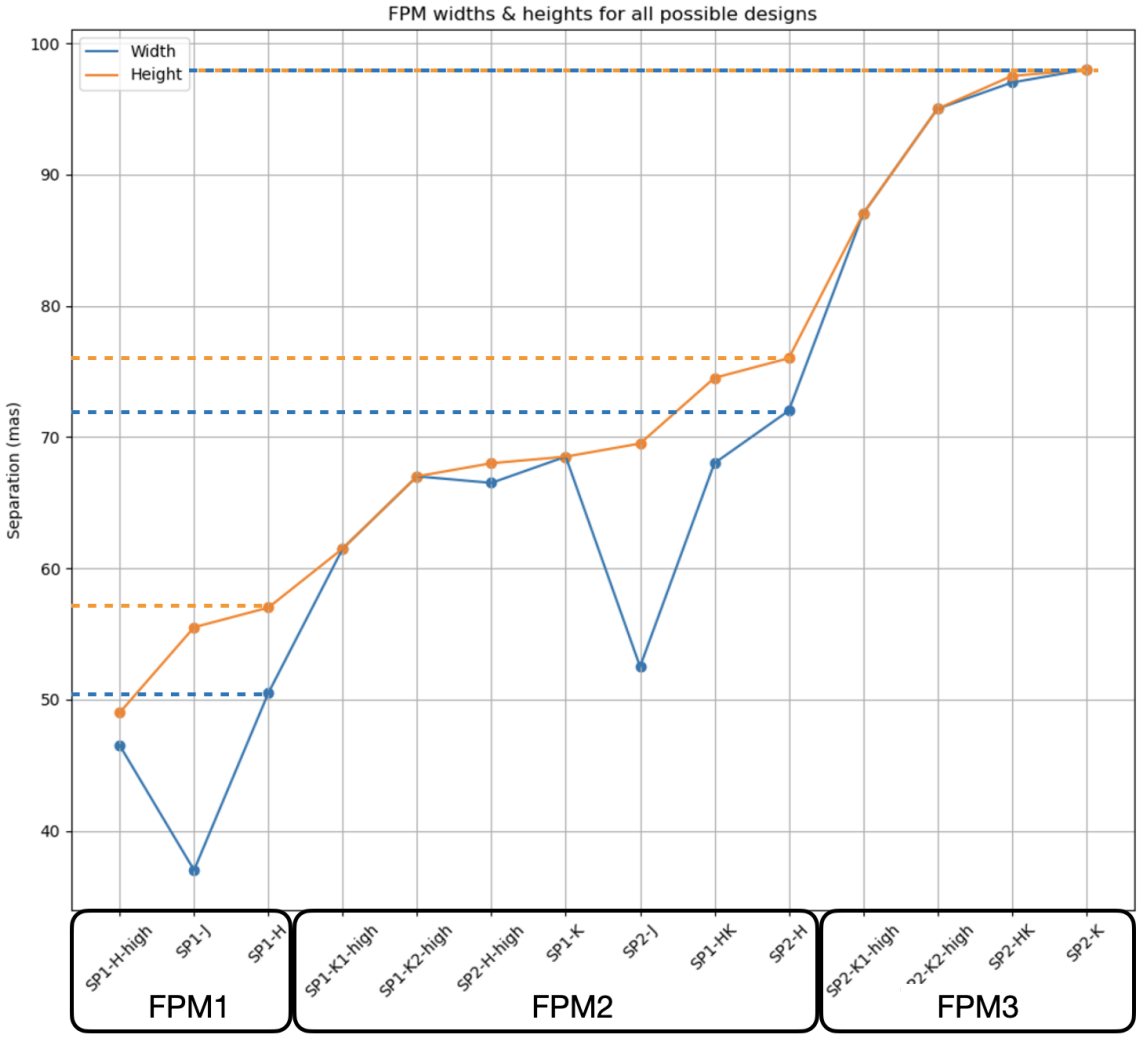

Figure 13: Ideal FPM sizes for each of the spectral range and apodizer combinations. Both the width and height are considered since dispersion forces the FPM to be elongated.

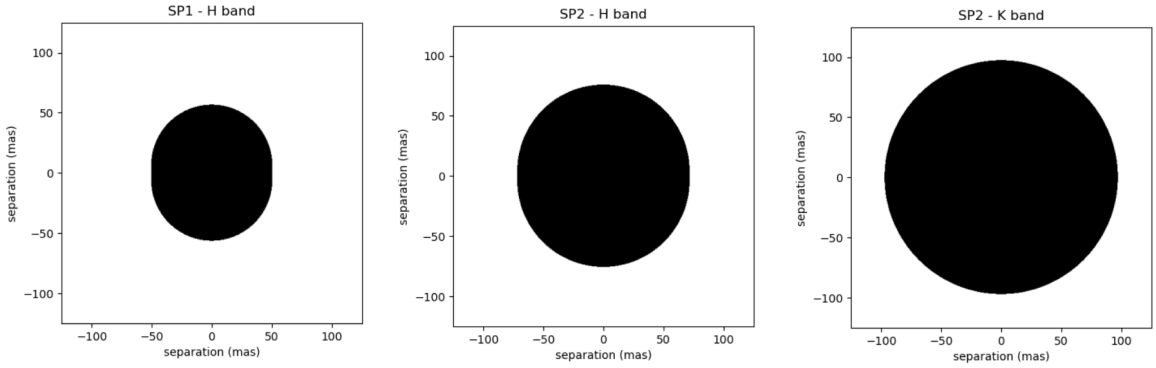

Figure 14: FPM patterns. The black region is associated with a 10^{-4} transmission.

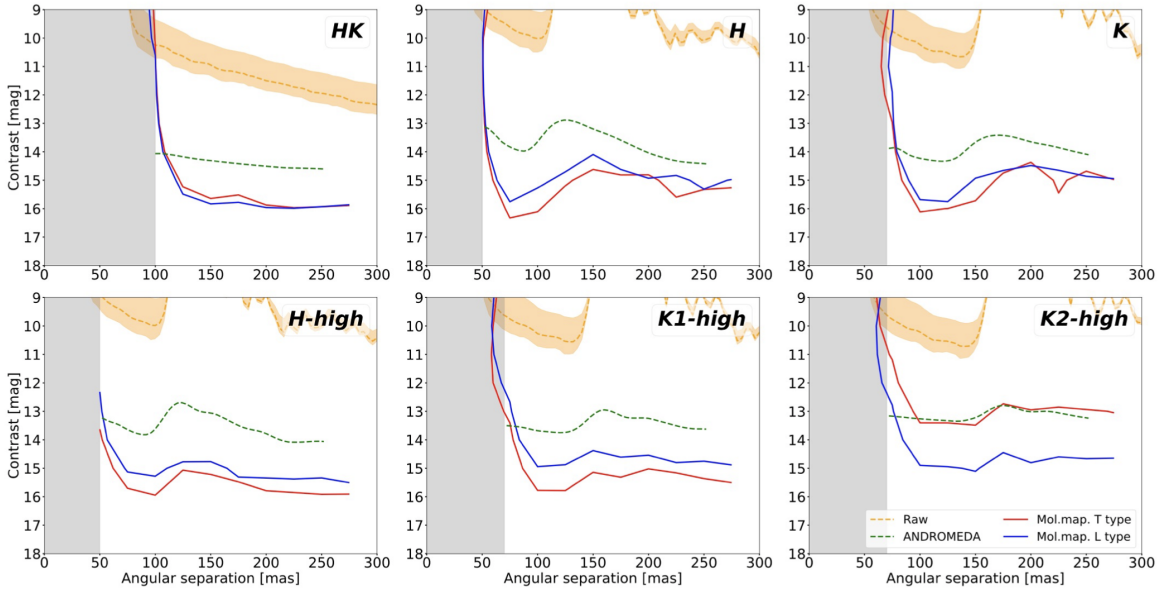

Figure 15: Detection limits obtained[17] with apodizer SP1 by processing the simulated data with ANDROMEDA and molecular mapping. The gray area denotes the presence of the FPM.

around the star that could potentially be used for observations will be masked when observing with either the SP1 apodizer or the SP2 apodizer.

4. EXPECTED PERFORMANCE

4.1 End-to-end model

The effective contrast limit has been estimated using mock-up datacubes obtained with an end-to-end model of HARMONI and of the HCM that takes into account both the performance of the SCAO mode, and the specifications of the HCM.

This model was described in two previous papers.[16,17] Its logic has not changed much since its latest presentation, and we refer the reader to these two publications for more details. The only updates that have been made are small design changes related to the apodizers and the FPM.

4.2 Detection limits after post-processing

Simulated datacubes in which fake planets were injected have been processed by both ANDROMEDA,[18] an algorithm that uses ADI, and by molecular mapping.[6,7] We reproduce here in fig.15 a series of plots[17] illustrating the contrast limit obtained by both post-processing methods in the HK, H, K, H high, K1 high, and K2 high spectral ranges.

In this study molecular mapping achieves a detection limit that is 1 to 2 magnitudes higher than ADI, up to a 16-16.5 delta magnitude at about 100mas from the star, except is the case of the K2 high spectral range when looking for a planet with a T-type spectrum, in which case their performance are very similar, and close to a 13.5 delta magnitude.

We have recently explored another approach to the estimation of the detection limit using molecular mapping. It does not use a large number of simulated datacubes representative of a typical observing sequence to be then processed as a real one would be.

This approach is instead semi-analytic. It assumes that given the application of the right high-pass filter in the Fourier-space of the wavelength domain, speckle noise can be attenuated enough that it becomes negligible. This assumption has been verified using data from the end-to-end model. The SNR can therefore be modeled analytically by considering only the photon noise of the diffracted light of the star (which is obtained from a

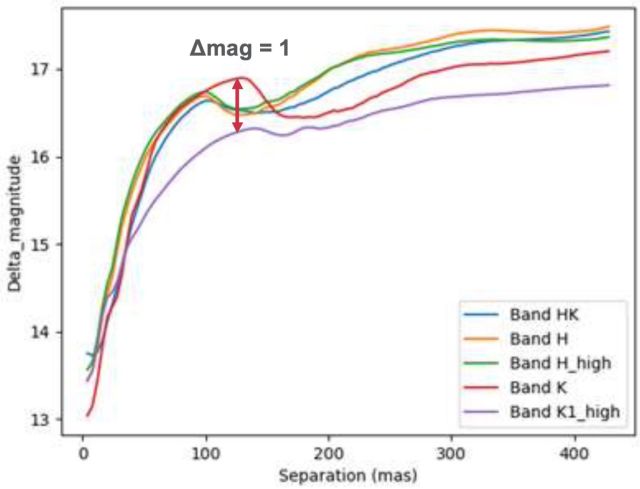

Figure 16: Detection limit with the SP1 apodizer in different spectral ranges using a fast, semi-analytical approach.

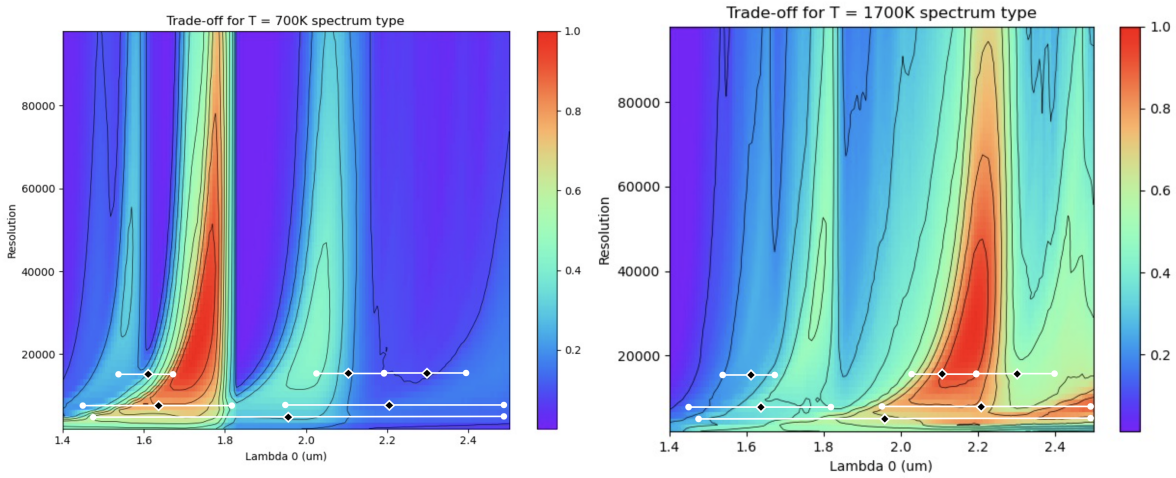

Figure 17: Normalized detectability of T=700K (left) and T=1700K (right) planets as a function of the central wavelength of a spectral range, and the resolving power. The same number of pixels as in HARMONI is assumed to be used to sample the data. The horizontal segments denote the spectral ranges of HARMONI.

single datacube obtained with the end-to-end model), the readout noise of the detector, and the background noise.

The detection limit is then derived from the SNR, and an example of the result of such an analysis is provided in fig.16. A 16-17 delta magnitude, i.e., a contrast of a few 10^{-7} is obtained at 100mas from the star.

This tool makes it quite easy to derive the exposure time that would be required to achieve a given contrast limit, and it may be used in the future as an efficient exposure time calculator for the HCM, assuming data will be processed through molecular mapping.

This tool is also capable of comparing the detectability of planets depending on their spectral type, or alternatively, their temperature, and while considering a continuum of resolving power and central wavelength for the spectral range. Assuming that the same number of pixels is used to sample the data for all of the spectral resolution modes that are considered, one can estimate in which conditions a planet should ideally be observed to be detected in the most efficient way.

Fig.17 illustrates this type of analysis for a T=700K planet, and a T=1700K planet. It shows that their detection can indeed be much more efficient if the right spectral range is selected. For instance, the T=700K

planet is preferentially detected using the H band spectral range, which has a R=7100 resolving power, and its detectability would be 10 times worse using the K band mode.

This points out the fact that while molecular mapping will be a great asset to detect planets, its efficiency may be quite sensitive to the observation mode that is selected, and that observations should be performed in several modes if possible.

5. CONCLUSION

A system analysis has been conducted to guide in the design of the HCM, i.e., the subsystem of ELT-HARMONI that will enable this first light, NIR IFU to image and characterize exoplanets.

The results of this analysis concern the surface error budget of the optics of HARMONI (in particular of the HCM), the specifications of the WFS in charge of sensing NCPA, and its planned operation, and the design of the pupil and image plane masks of the coronagraph, whose specifications may still slightly change up to the final design review that is scheduled in mid-2023.

A numerical model was developed to simulate datacubes similar to the ones that will be obtained with the instrument. The have been post-processed with ADI and molecular mapping algorithms. In the latter case, the result is that planets with a flux ratio of 10^{-6} may be detected as close as 50mas from the star, and with a flux ratio of a few 10^{-7} at 100mas.

This analysis completes two other publications presented at this conference, and which were focused on the design of the HCM, and on the prototyping activities of the ZELDA WFS that it will use.

ACKNOWLEDGMENTS

This work has been supported by the LabEx FOCUS (ANR-11-LABX-0013), and has received funding from the European Research Council (ERC) under the European Union's Horizon 2020 research and innovation programme (grant agreement n°866001).

REFERENCES

[1] Thatte, N., Tecza, M., Schnetler, H., Neichel, B., Melotte, D., Fusco, T., Ferraro-Wood, V., Clarke, F., Bryson, I., O'Brien, K., Mateo, M., Garcia Lorenzo, B., Evans, C., Bouché, N., Arribas, S., and HARMONI Consortium, "HARMONI: the ELT's First-Light Near-infrared and Visible Integral Field Spectrograph," *The Messenger* **182**, 7–12 (Mar. 2021).

[2] Beuzit, J. L., Vigan, A., Mouillet, D., Dohlen, K., Gratton, R., Boccaletti, A., Sauvage, J. F., Schmid, H. M., Langlois, M., Petit, C., Baruffolo, A., Feldt, M., Milli, J., Wahhaj, Z., Abe, L., Anselmi, U., Antichi, J., Barette, R., Baudrand, J., Baudoz, P., Bazzon, A., Bernardi, P., Blanchard, P., Brast, R., Bruno, P., Buey, T., Carbillet, M., Carle, M., Cascone, E., Chapron, F., Charton, J., Chauvin, G., Claudi, R., Costille, A., De Caprio, V., de Boer, J., Delboulbé, A., Desidera, S., Dominik, C., Downing, M., Dupuis, O., Fabron, C., Fantinel, D., Farisato, G., Feautrier, P., Fedrigo, E., Fusco, T., Gigan, P., Ginski, C., Girard, J., Giro, E., Gisler, D., Gluck, L., Gry, C., Henning, T., Hubin, N., Hugot, E., Incorvaia, S., Jaquet, M., Kasper, M., Lagadec, E., Lagrange, A. M., Le Coroller, H., Le Mignant, D., Le Ruyet, B., Lessio, G., Lizon, J. L., Llored, M., Lundin, L., Madec, F., Magnard, Y., Marteaud, M., Martinez, P., Maurel, D., Ménard, F., Mesa, D., Möller-Nilsson, O., Moulin, T., Moutou, C., Origné, A., Parisot, J., Pavlov, A., Perret, D., Pragt, J., Puget, P., Rabou, P., Ramos, J., Reess, J. M., Rigal, F., Rochat, S., Roelfsema, R., Rousset, G., Roux, A., Saisse, M., Salasnich, B., Santambrogio, E., Scuderi, S., Segransan, D., Sevin, A., Siebenmorgen, R., Soenke, C., Stadler, E., Suarez, M., Tiphène, D., Turatto, M., Udry, S., Vakili, F., Waters, L. B. F. M., Weber, L., Wildi, F., Zins, G., and Zurlo, A., "SPHERE: the exoplanet imager for the Very Large Telescope," *Astronomy and Astrophysics* **631**, A155 (Nov. 2019).

[3] Macintosh, B., Chilcote, J. K., Bailey, V. P., de Rosa, R., Nielsen, E., Norton, A., Poyneer, L., Wang, J., Ruffio, J. B., Graham, J. R., Marois, C., Savransky, D., and Veran, J.-P., "The Gemini Planet Imager: looking back over five years and forward to the future," in [*Adaptive Optics Systems VI*], Close, L. M., Schreiber, L., and Schmidt, D., eds., *Society of Photo-Optical Instrumentation Engineers (SPIE) Conference Series* **10703**, 107030K (July 2018).

[4] Ahn, K., Guyon, O., Lozi, J., Vievard, S., Deo, V., Skaf, N., Belikov, R., Bos, S. P., Bottom, M., Currie, T., Frazin, R., V. Gorkom, K., Groff, T. D., Haffert, S. Y., Jovanovic, N., Kawahara, H., Kotani, T., Males, J. R., Martinache, F., Mazin, B., Miller, K., Norris, B., Rodack, A., and Wong, A., "SCExAO: a testbed for developing high-contrast imaging technologies for ELTs," in [*Society of Photo-Optical Instrumentation Engineers (SPIE) Conference Series*], *Society of Photo-Optical Instrumentation Engineers (SPIE) Conference Series* **11823**, 1182303 (Sept. 2021).

[5] Males, J. R., Close, L. M., Miller, K., Schatz, L., Doelman, D., Lumbres, J., Snik, F., Rodack, A., Knight, J., Van Gorkom, K., Long, J. D., Hedglen, A., Kautz, M., Jovanovic, N., Morzinski, K., Guyon, O., Douglas, E., Follette, K. B., Lozi, J., Bohlman, C., Durney, O., Gasho, V., Hinz, P., Ireland, M., Jean, M., Keller, C., Kenworthy, M., Mazin, B., Noenickx, J., Alfred, D., Perez, K., Sanchez, A., Sauve, C., Weinberger, A., and Conrad, A., "MagAO-X: project status and first laboratory results," in [*Adaptive Optics Systems VI*], Close, L. M., Schreiber, L., and Schmidt, D., eds., *Society of Photo-Optical Instrumentation Engineers (SPIE) Conference Series* **10703**, 1070309 (July 2018).

[6] Snellen, I., de Kok, R., Birkby, J. L., Brandl, B., Brogi, M., Keller, C., Kenworthy, M., Schwarz, H., and Stuik, R., "Combining high-dispersion spectroscopy with high contrast imaging: Probing rocky planets around our nearest neighbors," *Astronomy and Astrophysics* **576**, A59 (Apr. 2015).

[7] Hoeijmakers, H. J., Schwarz, H., Snellen, I. A. G., de Kok, R. J., Bonnefoy, M., Chauvin, G., Lagrange, A. M., and Girard, J. H., "Medium-resolution integral-field spectroscopy for high-contrast exoplanet imaging. Molecule maps of the β Pictoris system with SINFONI," *Astronomy and Astrophysics* **617**, A144 (Oct. 2018).

[8] Haffert, S. Y., Bohn, A. J., de Boer, J., Snellen, I. A. G., Brinchmann, J., Girard, J. H., Keller, C. U., and Bacon, R., "Two accreting protoplanets around the young star PDS 70," *Nature Astronomy* **3**, 749–754 (June 2019).

[9] N'Diaye, M., Dohlen, K., Fusco, T., and Paul, B., "Calibration of quasi-static aberrations in exoplanet direct-imaging instruments with a Zernike phase-mask sensor," *Astronomy and Astrophysics* **555**, A94 (July 2013).

[10] Carlotti, A., Vanderbei, R., and Kasdin, N. J., "Optimal pupil apodizations of arbitrary apertures for high-contrast imaging," *Optics Express* **19**, 26796 (Dec. 2011).

[11] Hénault, F., Carlotti, A., Rabou, P., Magnard, Y., Sradler, E., Mouillet, D., Chauvin, G., Bonnefoy, M., Sauvage, J. F., Dohlen, K., Vigan, A., Fusco, T., El Hadi, K., Vola, P., Clarke, F., Thatte, N., Bryson, I., Schnetler, H., Tecza, M., and Vérinaud, C., "Opto-mechanical design of a High Contrast Module (HCM) for HARMONI," in [*Ground-based and Airborne Instrumentation for Astronomy VII*], Evans, C. J., Simard, L., and Takami, H., eds., *Society of Photo-Optical Instrumentation Engineers (SPIE) Conference Series* **10702**, 107028N (July 2018).

[12] Marafatto, L., Bergomi, M., Biondi, F., Carolo, E., De Pascale, M., Greggio, D., Lessio, L., Mesa, D., Radhakrishnan Santhakumari, K. K., Umbriaco, G., Vassallo, D., Viotto, V., Bianco, A., Dima, M., D'Orazi, V., Grenz, P., Leisenring, J. M., Mohr, L., Montoya, M., Zanutta, A., Antoniucci, S., Arcidiacono, C., Bacciotti, F., Baffa, C., Baruffolo, A., Bongiorno, A., Carlotti, A., Chinellato, S., Close, L., Di Filippo, S., Esposito, S., Farisato, G., Guyon, O., Hinz, P., Magrin, D., Pedichini, F., Pinna, E., Portaluri, E., Puglisi, A., Ragazzoni, R., Rossi, F., and Farinato, J., "SHARK-NIR, toward the installation at the Large Binocular Telescope," in [*Society of Photo-Optical Instrumentation Engineers (SPIE) Conference Series*], *Society of Photo-Optical Instrumentation Engineers (SPIE) Conference Series* **11448**, 114481M (Dec. 2020).

[13] Mennesson, B., Bailey, V. P., Zellem, R., Zimmerman, N., Ygouf, M., Hildebrandt, S., Rhodes, J., Kasdin, J., Macintosh, B., Turnbull, M., Douglas, E., Mandell, A., Nemati, B., Gonzalez, G., Cady, E., Kern, B., Krist, J., Shi, F., Mok, F., Morrissey, P., Heydorff, K., Pobereszhskiy, I., Zhao, F., Luchik, T., Maier, E. R., Akeson, R., Armus, L., Ingalls, J., Lowrance, P., and Meshkat, T., "The Roman Space Telescope coronagraph technology demonstration: current status and relevance to future missions," in [*Society of Photo-Optical Instrumentation Engineers (SPIE) Conference Series*], *Society of Photo-Optical Instrumentation Engineers (SPIE) Conference Series* **11823**, 1182310 (Sept. 2021).

[14] Krist, J. E., "PROPER: an optical propagation library for IDL," in [*Optical Modeling and Performance Predictions III*], Kahan, M. A., ed., *Society of Photo-Optical Instrumentation Engineers (SPIE) Conference Series* **6675**, 66750P (Sept. 2007).

[15] Vigan, A., Dohlen, K., N'Diaye, M., Cantalloube, F., Girard, J. H., Milli, J., Sauvage, J. F., Wahhaj, Z., Zins, G., Beuzit, J. L., Caillat, A., Costille, A., Le Merrer, J., Mouillet, D., and Tourenq, S., "Calibration of quasi-static aberrations in exoplanet direct-imaging instruments with a Zernike phase-mask sensor. IV. Temporal stability of non-common path aberrations in VLT/SPHERE," *Astronomy and Astrophysics* **660**, A140 (Apr. 2022).

[16] Carlotti, A., Hénault, F., Dohlen, K., Sauvage, J.-F., Rabou, P., Magnard, Y., Vigan, A., Mouillet, D., Chauvin, G., Vola, P., Bonnefoy, M., Fusco, T., El Hadi, K., Thatte, N., Clarke, F., Tecza, M., Bryson, I., Schnetler, H., and Vérinaud, C., "System analysis and expected performance of a high-contrast module for HARMONI," in [*Ground-based and Airborne Instrumentation for Astronomy VII*], Evans, C. J., Simard, L., and Takami, H., eds., *Society of Photo-Optical Instrumentation Engineers (SPIE) Conference Series* **10702**, 107029N (July 2018).

[17] Houllé, M., Vigan, A., Carlotti, A., Choquet, É., Cantalloube, F., Phillips, M. W., Sauvage, J. F., Schwartz, N., Otten, G. P. P. L., Baraffe, I., Emsenhuber, A., and Mordasini, C., "Direct imaging and spectroscopy of exoplanets with the ELT/HARMONI high-contrast module," *Astronomy and Astrophysics* **652**, A67 (Aug. 2021).

[18] Cantalloube, F., Mouillet, D., Mugnier, L. M., Milli, J., Absil, O., Gomez Gonzalez, C. A., Chauvin, G., Beuzit, J. L., and Cornia, A., "Direct exoplanet detection and characterization using the ANDROMEDA method: Performance on VLT/NaCo data," *Astronomy and Astrophysics* **582**, A89 (Oct. 2015).